Inorg. Chem. **2003**, *42*, 8406–8416

Interlayer Interaction of Two-Dimensional Layered Spin Crossover Complexes $[Fe^{II}H_3L^{Me}][Fe^{II}L^{Me}]X$ ($X^- = ClO_4^-$, BF_4^-, PF_6^-, AsF_6^-, and SbF_6^-; H_3L^{Me} = Tris[2-(((2-methylimidazol-4-yl)methylidene)amino)ethyl]amine)

Masahiro Yamada,[†] Makoto Ooidemizu,[†] Yuichi Ikuta,[†] Shutaro Osa,[†] Naohide Matsumoto,*[,†] Seiichiro Iijima,[‡] Masaaki Kojima,[§] Françoise Dahan,[||] and Jean-Pierre Tuchagues[||]

Department of Chemistry, Faculty of Science, Kumamoto University, Kurokami 2-39-1, Kumamoto 860-8555, Japan, National Institute of Advanced Industrial Science and Technology, Tsukuba 305-8566, Japan, Department of Chemistry, Faculty of Science, Okayama University, Tsushima-naka 3-1-1, Okayama 700-8530, Japan, and Laboratoire de Chimie de Coordination du CNRS, UP 8241, 205 Route de Narbonne, 31077 Toulouse Cedex 4, France

Received April 24, 2003

A series of two-dimensional (2D) spin crossover complexes, $[Fe^{II}H_3L^{Me}][Fe^{II}L^{Me}]X$ ($X^- = ClO_4^-$, BF_4^-, PF_6^-, AsF_6^-, SbF_6^-) **1**–**5**, have been synthesized, where H_3L^{Me} denotes an hexadentate N_6 tripodlike ligand containing three imidazole groups, tris[2-(((2-methylimidazol-4-yl)methylidene)amino)ethyl]amine. Compounds **1**–**5** exhibit a two-step (HS-$[Fe^{II}H_3L^{Me}]^{2+}$ + HS-$[Fe^{II}L^{Me}]^-$) ↔ (HS-$[Fe^{II}H_3L^{Me}]^{2+}$ + LS-$[Fe^{II}L^{Me}]^-$) ↔ (LS-$[Fe^{II}H_3L^{Me}]^{2+}$ + LS-$[Fe^{II}L^{Me}]^-$) spin-transition. The crystal structure of $[Fe^{II}H_3L^{Me}][Fe^{II}L^{Me}]PF_6$ (**3**) was determined at 295, 200, and 100 K. The structure consists of homochiral extended 2D puckered sheets, in which the complementary $[Fe^{II}H_3L^{Me}]^{2+}$ and $[Fe^{II}L^{Me}]^-$ capped tripodlike components, linked together by imidazole–imidazolate hydrogen bonds, are alternately arrayed in an up-and-down mode. The Fe–N bond distances and angles revealed that the Fe^{II} sites of both constituting units are in the high-spin (HS) state at 295 K; at 200 K, the Fe^{II} sites of $[Fe^{II}H_3L^{Me}]^{2+}$ and $[Fe^{II}L^{Me}]^-$ are in the HS and low-spin (LS) states, respectively. The Fe^{II} sites of both constituting units are in the LS state at 100 K. The size of the counteranion affects significantly the intra- and interlayer interactions leading to modifications of the spin crossover behavior. The onset of the second spin-transition of the ClO_4^- (**1**) and BF_4^- (**2**) salts adjoins the first spin-transition, while a mixed (HS-$[Fe^{II}H_3L^{Me}]^{2+}$ + LS-$[Fe^{II}L^{Me}]^-$) spin-state spans a temperature range as wide as 70 K for salts **3**–**5** with larger counteranions, PF_6^-, AsF_6^-, and SbF_6^-, respectively. Compounds **1** and **2** showed remarkable LIESST (light induced excited spin state trapping) and reverse-LIESST effects, whereas **3**–**5** showed no remarkable LIESST effect. The interlayer interaction due to the size of the counteranion is an important factor governing the spin crossover behavior and LIESST effect.

Introduction

Increasing attention has been devoted to multifunctional magnetic materials such as light-induced magnets,[1] electric conductive magnets,[2] and guest-absorbed magnetic switches,[3] in which different magnetic and electronic properties are interconverted by different external perturbations. Spin crossover (SCO) compounds[4] are the most spectacular and representative examples of molecular bistability. SCO between the low-spin (LS) and high-spin (HS) states is observed in some octahedral $3d^n$ ($4 \leq n \leq 7$) metal complexes and is induced by an external perturbation, such as temperature, pressure, or light irradiation. Since the discovery of LIESST

* To whom correspondence should be addressed. E-mail: naohide@aster.sci.kumamoto-u.ac.jp. Fax: +81-96-342-3390.

[†] Kumamoto University.

[‡] National Institute of Advanced Industrial Science and Technology, Tsukuba.

[§] Okayama University.

[||] Laboratoire de Chimie de Coordination du CNRS Toulouse.

(1) (a) Ohkoshi, S.; Hashimoto, K. *J. Am. Chem. Soc.* **1999**, *121*, 10591−10597. (b) Sato, O.; Iyoda, T.; Fujishima, A.; Hashimoto, K. *Science* **1996**, *272*, 704−705.

(2) (a) Coronado, E.; Galan-Mascaros, J. R.; Gomez-Garcia, C. J.; Laukhin, V. *Nature* **2000**, *408*, 447−449. (b) Takamatsu, N.; Akutagawa, T.; Hasegawa, T.; Nakamura, T.; Inabe, T.; Fujita, W.; Awaga, K. *Inorg. Chem.* **2000**, *39*, 870−871. (c) Imai, H.; Otsuka, T.; Naito, T.; Awaga, K.; Inabe, T. *J. Am. Chem. Soc.* **1999**, *121*, 8098−8103.

(3) Halder, G. J.; Kepert, C. J.; Moubaraki, B.; Murray, K. S.; Cashion, J. D. *Science* **2002**, *298*, 1762−1765.

10.1021/ic034439e CCC: $25.00
Published on Web 11/08/2003

(light induced excited spin state trapping) and reverse-LIESST effects,[5] the photoswitchable SCO compounds with long-lived metastable states and large hysteresis are of current interest.[6] It is now well established that the elastic interactions between SCO sites govern the bistability, while SCO itself is essentially a single molecule phenomenon. From this viewpoint, recent efforts have been devoted to design and synthesize SCO compounds exhibiting strong elastic interactions between spin-transition sites. Polymeric SCO compounds with bridging ligands[7] and mononuclear SCO compounds exhibiting intermolecular interactions such as hydrogen bonding and $\pi-\pi$ stacking[8] have been extensively investigated.

Previously, we have reported an unprecedented homochiral mixed-valence SCO complex, $[Fe^{II}H_3L][Fe^{III}L](NO_3)_2$ (H_3L = tris-[2-(((imidazol-4-yl)methylidene)amino)ethyl]amine), and shown that (1) the tripodlike ligand containing three imidazole groups is the first ligand affording SCO behavior for both the Fe^{II} and Fe^{III} oxidation states, and (2) the 2D extended network structure based on imidazole−imidazolate hydrogen bonds produces elastic interactions between SCO sites.[9a] In a previous paper,[9b] we have investigated how the degree of deprotonation at the imidazole moiety and the substituent effect govern the oxidation and spin states. In this study, in order to investigate the effect of interlayer interactions, we analyze how the counteranion modifies the SCO behavior of these 2D complexes through interlayer elastic interactions (see Scheme 1). To this purpose, we have synthesized a series of $[Fe^{II}H_3L^{Me}][Fe^{II}L^{Me}]X$ complexes with counteranions of various sizes ($X^- = ClO_4^-$, BF_4^-, PF_6^-, AsF_6^-, SbF_6^-) **1**−**5**. On the basis of their syntheses, crystal structures, magnetic, and photomagnetic properties, we report here how the size of the counteranion governs the SCO behavior of these 2D complexes through interlayer interactions.

Scheme 1. Schematic Drawing of a 2D Layered Complex[a]

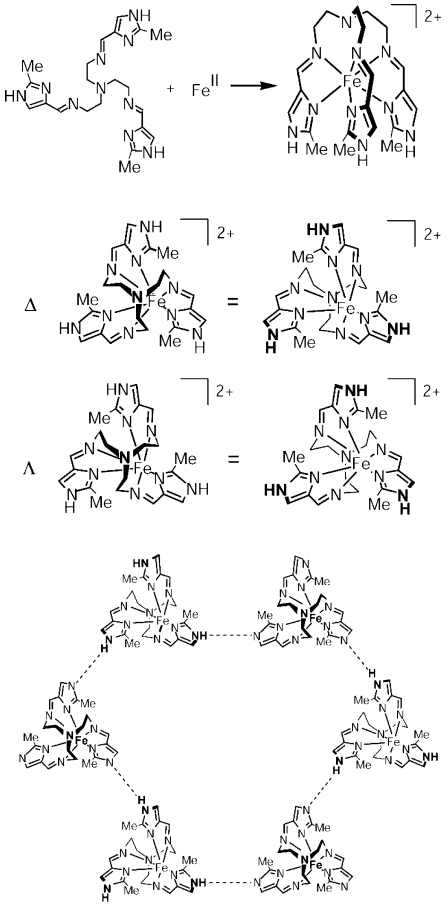

[a] Coordination of the achiral tripod ligand H_3L^{Me} to the transition metal ion yields Δ (clockwise) and Λ (anticlockwise) chiral molecule $[Fe^{II}H_3L^{Me}]^{2+}$ due to its screw coordination arrangement. The generated chiral complementary components $[Fe^{II}H_3L^{Me}]^{2+}$ and $[Fe^{II}L^{Me}]^-$ are assembled by imidazole−imidazolate hydrogen bonds into a homochiral 2D sheet based on the $\{[Fe^{II}H_3L^{Me}][Fe^{II}L^{Me}]\}_3$ hexameric unit.

Results and Discussion

Synthesis and Characterization of 2D Layered Complexes $[Fe^{II}H_3L^{Me}][Fe^{II}L^{Me}]X$ ($X^- = ClO_4^-$, BF_4^-, PF_6^-, AsF_6^-, SbF_6^-) (1−5). The Fe^{II} complexes with the neutral ligand form, $[Fe^{II}H_3L^{Me}]X_2$ ($X^- = ClO_4^-$, BF_4^-) (**1a**, **2a**) and $[Fe^{II}H_3L^{Me}]Cl\cdot X$ ($X^- = PF_6^-$, AsF_6^-, SbF_6^-) (**3a, 4a, 5a**), were obtained as orange and dark-orange crystals, respectively, from the mixed solution of the ligand H_3L^{Me}, $Fe^{II}Cl_2\cdot 4H_2O$, and NaX or KX at the 1:1:2 molar ratio in methanol under aerobic condition. The Fe^{II} complex cation with the neutral ligand, $[Fe^{II}H_3L^{Me}]^{2+}$, associated to a small

(4) (a) König, E. *Prog. Inorg. Chem.* **1987**, *35*, 527−623. (b) König, E. *Struct. Bonding* (*Berlin*) **1991**, *76*, 51. (c) Goodwin, H. A. *Coord. Chem. Rev.* **1976**, *18*, 293−325. (d) Gütlich, P.; Hauser, A.; Spiering, H. *Angew. Chem., Int. Ed. Engl.* **1994**, *33*, 2024−2054.

(5) (a) Decurtins, S.; Gütlich, P.; Kohler, C. P.; Spiering, H.; Hauser, A. *Chem. Phys. Lett.* **1984**, *105*, 1−4. (b) Decurtins, S.; Gütlich, P.; Hasselbach, K. M.; Hauser, A.; Spiering, H. *Inorg. Chem.* **1985**, *24*, 2174−2178. (c) Gütlich, P.; Garcia, Y.; Woike, T. *Coord. Chem. Rev.* **2001**, *219*−*221*, 839−879.

(6) (a) Kahn, O.; Martinez, J. C. *Science* **1998**, *279*, 44−48. (b) van Koningsbruggen, P. J.; Garcia, Y.; Kahn, O.; Fournes, L.; Kooijman, H.; Spek, A. L.; Haasnoot, J. G.; Moscovici, J.; Provost, K.; Michalowicz, A.; Renz, F.; Gütlich, P. *Inorg. Chem.* **2000**, *39*, 1891−1900. (c) Real, J. A.; Andres, E.; Munoz, M. C.; Julve, M.; Granier, T.; Bousseksou, A.; Varret, F. *Science* **1995**, *268*, 265−267.

(7) (a) Letard, J.-F.; Guionneau, P.; Rabardel, L.; Howard, J. A. K.; Goeta, A. E.; Chasseau, D.; Kahn, O. *Inorg. Chem.* **1998**, *37*, 4432−4441. (b) Garcia, Y.; Kahn, O.; Rabardel, L.; Chansou, B.; Salmon, L.; Tuchagues, J.-P. *Inorg. Chem.* **1999**, *38*, 4663−4670. (c) Breuning, E.; Ruben, M.; Lehn, J.-M.; Renz, F.; Garcia, Y.; Ksenofontov, V.; Gütlich, P.; Wegelius, E.; Rissanen, K. *Angew. Chem., Int. Ed.* **2000**, *39*, 2504−2507. (d) Moliner, N.; Munoz, C.; Letard, S.; Solans, X.; Menendez, N.; Goujon, A.; Varret, F.; Real, J. A. *Inorg. Chem.* **2000**, *39*, 5390−5393. (e) Petrouleas, V.; Tuchagues, J.-P. *Chem. Phys. Lett.* **1987**, *137*, 21−25. (f) Rakotonandrasana, A. S.; Boinnard, D.; Petrouleas, V.; Cartier, C.; Verdaguer, M.; Savariault, J.-M.; Tuchagues, J.-P. *Inorg. Chim. Acta* **1991**, *180*, 19−31. (g) Boinnard, D.; Bousseksou, A.; Dworkin, A.; Savariault, J.-M.; Varret, F.; Tuchagues, J.-P. *Inorg. Chem.* **1994**, *33*, 271−281. (h) Bousseksou, A.; Tommasi, L.; Lemercier, G.; Varret, F.; Tuchagues, J.-P. *Chem. Phys. Lett.* **1995**, *243*, 493−499. (i) Bousseksou, A.; Salmon, L.; Varret, F.; Tuchagues, J.-P. *Chem. Phys. Lett.* **1998**, *282*, 209−214. (j) Salmon, L.; Donnadieu, B.; Bousseksou, A.; Tuchagues, J.-P. *C. R. Acad. Sci., Ser. IIc: Chim.* **1999**, 305−309.

(8) (a) Hayami, S.; Gu, Z.; Shiro, M.; Einaga, A.; Fujishima, A.; Sato, O. *J. Am. Chem. Soc.* **2000**, *122*, 7126−7127. (b) Hayami, S.; Gu, Z.; Yoshiki, H.; Fujishima, A.; Sato, O. *J. Am. Chem. Soc.* **2001**, *123*, 11644−11650. (c) Boca, R.; Boca, M.; Dihan, L.; Falk, K.; Fuess, H.; Haase, W.; Jarosciak, R.; Papankova, B.; Renz, F.; Vrbova, M.; Werner, R. *Inorg. Chem.* **2001**, *40*, 3025−3033.

(9) (a) Sunatsuki, Y.; Ikuta, Y.; Matsumoto, N.; Ohta, H.; Kojima, M.; Iijima, S.; Hayami, S.; Maeda, Y.; Kaizaki, S.; Dahan, F.; Tuchagues, J.-P. *Angew. Chem., Int. Ed.* **2003**, 42, 1614−1618. (b) Ikuta Y.; Ooidemizu, M.; Yamahata, Y.; Yamada, M.; Osa, S.; Matsumoto, N.; Iijima, S.; Sunatsuki, Y.; Kojima, M.; Dahan, F.; Tuchagues, J.-P. *Inorg. Chem.* **2003**, *42*, 7001−7017.

counteranion such as ClO_4^- and BF_4^- crystallized with the chemical formula $[Fe^{II}H_3L^{Me}]X_2$, while the complex cation associated to larger counteranions such as PF_6^-, AsF_6^-, and SbF_6^- crystallized with the chemical formula $[Fe^{II}H_3L^{Me}]Cl\cdot X$.

Addition of 1 M aqueous KOH to the Fe^{II} complexes with the neutral ligand **1a**−**5a** in methanol (1:1.5 molar ratio) in the air yielded red-black crystals with the formula $[Fe^{II}H_3L^{Me}][Fe^{II}L^{Me}]X$ (**1**−**5**): deprotonation of $[Fe^{II}H_3L^{Me}]^{2+}$ produces an acid−base reaction yielding $[Fe^{II}H_3L^{Me}]^{2+}$ and $[Fe^{II}L^{Me}]^-$ which assemble together into 2D sheets owing to imidazole−imidazolate hydrogen bonds, as described for analogous compounds.[10]

The infrared (IR) spectra for the series of Fe^{II} complexes **1a**−**5a** and 2D layered complexes **1**−**5** were measured at room temperature. All IR spectra for the complexes with the neutral ligand (**1a**−**5a**) showed a characteristic sharp single band at ca. 1640 cm^{-1} due to the C═N stretching vibration of the Schiff-base ligand assignable to the HS Fe^{II} state.[11] The 2D layered complexes **1**−**5** exhibit a deformed peak due to superimposition of the C═N stretching vibrations of the $[Fe^{II}H_3L^{Me}]^{2+}$ and $[Fe^{II}L^{Me}]^-$ components. The wavenumber of the deformed peak is close to ca. 1635 cm^{-1}, suggesting that the Fe^{II} of both $[Fe^{II}H_3L^{Me}]^{2+}$ and $[Fe^{II}L^{Me}]^-$ components is in the HS state at room temperature. Since the 2D layered complexes experience a two-step spin-transition as described in the magnetic property section, temperature dependent IR spectroscopy as well as laser Raman spectroscopy will provide valuable information on the SCO behavior.[12]

Crystal Structure of $[Fe^{II}H_3L^{Me}][Fe^{II}L^{Me}]PF_6$ (3). The X-ray structural analysis of **3** was performed at 295, 200, and 100 K, because the magnetic data demonstrated that the Fe^{II} sites of **3** are all in the HS state at 295 K, in the 1:1 HS/LS ratio at 200 K, and both in the LS state at 100 K. There are several possible chemical formulations regarding the imidazole hydrogen position such as $[Fe^{II}H_3L^{Me}]^{2+}$-$[Fe^{II}L^{Me}]^-(PF_6^-)$, $[Fe^{II}H_{1.5}L^{Me}]^{0.5}[Fe^{II}H_{1.5}L^{Me}]^{0.5}(PF_6^-)$, and $[Fe^{II}H_2L^{Me}]^+[Fe^{II}HL^{Me}]^0(PF_6^-)$. The X-ray analysis is not fully reliable to determine the hydrogen atoms, but we reached a conclusion for one chemical formulation on the basis of the following description in related studies.[9,10a] The imidazole hydrogen atom H(7) has been located on the D-Fourier at all three temperatures, and subsequent satisfactory refinement of H(7) allowed us to conclude the $[Fe^{II}H_3L^{Me}]^{2+}[Fe^{II}L^{Me}]^-(PF_6^-)$ formulation. Although not only the imidazole hydrogen atom but also approximately half of all hydrogen atoms were located on successive D-Fourier series, for consistency, all hydrogen atoms were placed at the geometrically ideal positions for the CIF file. The crystallographic data are summarized in Table 1. The crystal system and the space group are the same at all three temperatures, suggesting that there is no first-order phase-transition associated with the SCO. Selected bond distances, angles, and hydrogen bond distances with their estimated standard deviations in parentheses are given in Table 2. Figure 1 shows the ORTEP drawing of the molecular structure of the hydrogen-bonded $\{[Fe^{II}H_3L^{Me}]^{2+}\cdots[Fe^{II}L^{Me}]^-\}$ constituting units with the atom numbering at 100 K, where the thermal ellipsoids are drawn at 50% probability level. Figure 2a,b shows the top and side views of a 2D puckered sheet, respectively.

Table 1. X-ray Crystallographic Data for $[Fe^{II}H_3L^{Me}][Fe^{II}L^{Me}]PF_6$ (**3**) at 295, 200, and 100 K

	295 K	200 K	100 K
formula	$C_{42}H_{57}F_6Fe_2N_{20}P$	$C_{42}H_{57}F_6Fe_2N_{20}P$	$C_{42}H_{57}F_6Fe_2N_{20}P$
fw	1098.75	1098.75	1098.75
cryst syst	trigonal	trigonal	trigonal
space group	*R*3 (No. 146)	*R*3 (No. 146)	*R*3 (No. 146)
a, Å	12.486(2)	12.3152(11)	12.1525(17)
b, Å	12.486(2)	12.3152(11)	12.1525(17)
c, Å	27.783(4)	27.424(3)	27.742(3)
V, Å^3	3751.1(12)	3602.0(6)	3465.8(8)
Z	3	3	3
T, K	295 ± 2	200 ± 2	100 ± 2
D_{calcd}, Mg m^{-3}	1.459	1.520	1.579
μ(Mo Kα), mm^{-1}	0.689	0.717	0.745
data collected	9397	8943	8507
unique data	3192	3057	2906
obsd reflns[a]	1852	2670	2596
R^b obsd, all	0.0391, 0.0707	0.0375, 0.0405	0.0391, 0.0417
$R_w{}^c$ obsd, all	0.0716, 0.0791	0.0795, 0.0807	0.0800, 0.0813
S	0.799	1.006	0.988
(Δ/ρ)max, min [e Å^{-3}]	0.292, −0.235	1.025, −0.240	0.375, −0.319

[a] Data with $F_o > 4\sigma(F_o)$. [b] $R = \sum||F_o| - |F_c||/\sum|F_o|$. [c] $R_w = [\sum w(|F_o^2| - |F_c^2|)^2/\sum w|F_o^2|^2]^{1/2}$.

Both Fe(2) ($[Fe^{II}H_3L^{Me}]^{2+}$) and Fe(1) ($[Fe^{II}L^{Me}]^-$) assume an octahedral coordination environment with 6 N donor atoms. Both $[Fe^{II}H_3L^{Me}]^{2+}$ and $[Fe^{II}L^{Me}]^-$ components are chiral with either Δ (clockwise) or Λ (anticlockwise) configuration due to the screw coordination arrangement of the achiral tripod ligand around Fe^{II}. Both components act as chiral complementary building units assembling into a 2D extended structure due to the imidazole−imidazolate hydrogen bonds. In this 2D supramolecular structure, the capped tripodlike $[Fe^{II}H_3L^{Me}]^{2+}$ and $[Fe^{II}L^{Me}]^-$ components with the same chirality, connected through hydrogen bonds, are arrayed alternately in an up-and-down mode yielding a homochiral extended 2D puckered sheet, as shown in Figure 2a,b. Furthermore, adjacent sheets with the same chirality stack together forming a chiral crystal, as shown in Figure 2c. In the structure, one $\{[Fe^{II}H_3L^{Me}]^{2+}\cdots[Fe^{II}L^{Me}]^-\}$ pair is associated to one PF_6^- counteranion. The PF_6^- counteranions are located between the 2D sheets. The crystal structure indicates that spontaneous resolution took place during the

(10) (a) Katsuki, I.; Motoda, Y.; Sunatsuki, Y.; Matsumoto, N.; Nakashima, T.; Kojima, M. *J. Am. Chem. Soc.* **2002**, *124*, 629−640. (c) Mimura, M.; Matsuo, T.; Motoda, Y.; Matsumoto, N.; Nakashima, T.; Kojima, M. *Chem. Lett.* **1998**, 691−692. (b) Sunatsuki, Y.; Motoda, Y.; Matsumoto, N. *Coord. Chem. Rev.* **2002**, *226*, 199−209. (c) Shii, Y.; Motoda, Y.; Matsuo, T.; Kai, F.; Nakashima, T.; Tuchagues, J.-P.; Matsumoto, N. *Inorg. Chem.* **1999**, *38*, 3513−3522.

(11) Nakamoto, K. In *Infrared and Raman Spectra of Inorganic and Coordination Compounds*, 5th ed.; John Wiley and Sons: New York, 1997; Part B, Chapter III-14.

(12) (a) Zilverentant, C. L.; van Albada, G. A.; Bousseksou, A.; Haasnoot, J. G.; Reedijk, J. *Inorg. Chim. Acta* **2000**, *303*, 287−290. (b) Sunatsuki, Y.; Sakata, M.; Matsuzaki, S.; Matsumoto, N.; Kojima, M. *Chem. Lett.* **2001**, 1254−1255. (c) Suemura, N.; Ohama, M.; Kaizaki, S. *Chem. Commun.* **2001**, 1538−1539.

Table 2. Relevant Bond Lengths (Å), Angles (deg), and Hydrogen Bond Distances (Å) with Estimated Standard Deviations in Parentheses for $[Fe^{II}H_3L^{Me}][Fe^{II}L^{Me}]PF_6$ (**3**)[a]

	295 K	200 K	100 K
	Bond Lengths (Å)		
Fe(1)−N(1)	2.187(4)	1.987(3)	1.993(3)
Fe(1)−N(2)	2.175(3)	2.017(3)	2.006(3)
Fe(2)−N(5)	2.168(4	2.163(3)	1.987(3)
Fe(2)−N(6)	2.171(4)	2.188(3)	2.013(3)
N(1)−C(1)	1.277(6)	1.304(4)	1.296(4)
N(1)−C(6)	1.433(5)	1.452(4)	1.455(4)
N(2)−C(2)	1.381(5	1.394(4)	1.399(4)
N(2)−C(4)	1.334(5)	1.356(4)	1.330(4)
N(3)−C(3)	1.355(5)	1.374(4)	1.366(4)
N(3)−C(4)	1.348(6)	1.343(6)	1.372(4)
N(4)−C(7)	1.457(5)	1.430(3)	1.445(3)
C(1) −C(2)	1.426(7)	1.423(5	1.420(5)
C(2)−C(3)	1.381(6)	1.385(4)	1.383(4)
C(4)−C(5)	1.487(6)	1.477(4)	1.489(4)
C(6)−C(7)	1.512(6)	1.526(5)	1.532(5)
N(5)−C(8)	1.269(6)	1.277(4)	1.284(4)
N(5) −C(13	1.455(5)	1.469(4)	1.463(4)
N(6)−C(9)	1.387(5)	1.385(4)	1.399(4)
N(6)−C(11)	1.336(5)	1.292(4)	1.325(4)
N(7)−C(10)	1.348(5)	1.359(4)	1.364(4)
N(7)−C(11)	1.337(6)	1.371(4)	1.371(4)
N(8)−C(14)	1.436(5)	1.457(4)	1.441(3)
C(8)−C(9)	1.427(7)	1.434(5)	1.439(5)
C(9)−C(10)	1.354(6)	1.367(5)	1.363(4)
C(11)−C(12)	1.473(6)	1.490(5)	1.497(4)
C(13)−C(14)	1.534(7)	1.532(5)	1.529(5)
	Bond Angles (deg)		
N(1)−Fe(1)−N(2)	77.48(14)	81.41(11)	81.78(10)
N(1)−Fe(1)−N(1A)	97.14(13)	95.15(10)	95.02(10)
N(1) −Fe(1) −N(2A)	170.24(14)	174.34(11)	174.59(11)
N(1)−Fe(1)−N(2B)	91.65(13)	89.65(10)	89.62(10)
N(2)−Fe(1)−N(2A)	94.41(13)	94.04(10)	93.80(10)
N(5)−Fe(2)−N(6)	77.36(14)	77.65(10)	81.57(10)
N(5)−Fe(2)−N(5C)	97.18(14)	97.90(9)	95.05(10)
N(5)−Fe(2)−N(6C)	91.68(13)	91.16(10)	89.89(10)
N(5)−Fe(2)−N(6D)	170.15(14)	170.41(10)	174.26(11)
N(6)−Fe(2)−N(5D)	91.68(13)	91.16(10)	89.89(10)
N(6)−Fe(2)−N(6C)	94.47(13)	93.85(10)	93.75(10)
	Hydrogen Bonds (Å, deg)		
N(7)···N(3)	2.698(5)	2.684(4)	2.693(4)
N(7)−H(7)···N(3)	139.4	140.9	135.5

[a] Symmetry operations: A, $-x + y$, $1 - x$, z; B, $1 - y$, $1 + x - y$, z; C, $1 - x + y$, $1 - x$, z; D, $1 - y$, $x - y$, z.

course of the assembly reaction and crystallization.[13] In agreement with the X-ray structure, selected crystals show enantiomeric circular dichroism (CD) spectra, thus providing definitive evidence that spontaneous resolution has occurred.

The unit cell volume of 3751.1(12) $Å^3$ at 295 K is reduced to 3602.0(6) $Å^3$ at 200 K (4.0% reduction) and to 3465.8(8) $Å^3$ at 100 K (7.6% reduction). The reduction of the unit cell volume upon decrease in temperature is ascribed to the SCO. On the basis of the Fe−N bond distances and N−Fe−N bond angles, the SCO behavior of the two Fe^{II} sites can be well identified. At 295 K, the Fe(2)−N distances in $[Fe^{II}H_3L^{Me}]^{2+}$ are in the 2.168(4)−2.171(4) Å range, and the Fe(1)−N distances in $[Fe^{II}L^{Me}]^-$ are in the 2.175(3)−2.187(4) Å range, both typical for HS Fe^{II} bound to imine and imidazole nitrogen atoms. At 200 K, the Fe(2)−N distances in $[Fe^{II}H_3L^{Me}]^{2+}$ are in the 2.163(3)−2.188(3) Å range, typical

(13) (a) Jacques, J.; Collet, A.; Wilen, S. H. *Enantiomers, racemates and resolutions*; John Wiley & Sons: New York, 1981. (b) Katsuki, I.; Matsumoto, N.; Kojima, M. *Inorg. Chem.* **2000**, *39*, 3350−3354.

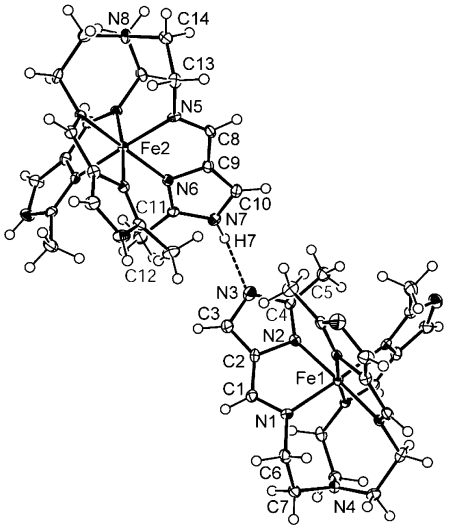

Figure 1. Molecular structure of $[Fe^{II}H_3L^{Me}][Fe^{II}L^{Me}]PF_6$ (**3**) 100 K with atom numbering scheme. The chiral complementary components $[Fe^{II}H_3L^{Me}]^{2+}$ (Fe2) and $[Fe^{II}L^{Me}]^-$ (Fe1) with the same chirality are connected by imidazole−imidazolate hydrogen bonds.

for HS Fe^{II}, while the Fe(1)−N distances in $[Fe^{II}L^{Me}]^-$ are in the 1.987(3)−2.017(3) Å range, typical for LS Fe^{II}. The decrease in the average Fe−N distances between 295 and 200 K is 0.006 and 0.179 Å for $[Fe^{II}H_3L^{Me}]^{2+}$ (Fe2) and $[Fe^{II}L^{Me}]^-$ (Fe1), respectively, demonstrating that, in the 295−200 K range, the SCO does not occur at Fe(2) ($[Fe^{II}H_3L^{Me}]^{2+}$) but at Fe(1) ($[Fe^{II}L^{Me}]^-$). The N−Fe−N bond angles change drastically in $[Fe^{II}L^{Me}]^-$, getting closer to a regular octahedron (for example, N(1)−Fe(1)−N(2), 77.48(14)° at 295 K, 81.41(11)° at 200 K), while the N−Fe(2)−N bond angles in $[Fe^{II}H_3L^{Me}]^{2+}$ showed no remarkable change (for example, N(5)−Fe(2)−N(6), 77.36(14)° at 295 K, 77.65(10)° at 200 K). At 100 K, the Fe(2)−N distances in $[Fe^{II}H_3L^{Me}]^{2+}$ are in the 1.987(3)−2.013(3) Å range and the Fe(1)−N distances in $[Fe^{II}L^{Me}]^-$ are in the 1.993(3)−2.006(3) Å range, both typical for LS Fe^{II}. The decrease in the average Fe−N distance between 200 and 100 K is 0.176 and 0.003 Å for Fe(2) ($[Fe^{II}H_3L^{Me}]^{2+}$) and Fe(1) ($[Fe^{II}L^{Me}]^-$), respectively, demonstrating that the SCO occurred at Fe(2) ($[Fe^{II}H_3L^{Me}]^{2+}$) in the 200−100 K range. The N−Fe(2)−N bond angles in $[Fe^{II}H_3L^{Me}]^{2+}$ change drastically, getting closer to those of a regular octahedron (for example, N(5)−Fe(2)−N(6), 77.65(10)° at 200 K, 81.57(10)° at 100 K), while those of $[Fe^{II}L^{Me}]^-$ show no substantial change (for example, N(1)−Fe(1)−N(2), 81.41(11)° at 200 K, 81.78(10)° at 100 K). The present X-ray analyses at 295, 200, and 100 K supply definitive evidence for the two-step (HS-$[Fe^{II}H_3L^{Me}]^{2+}$ + HS-$[Fe^{II}L^{Me}]^-$) ↔ (HS-$[Fe^{II}H_3L^{Me}]^{2+}$ + LS-$[Fe^{II}L^{Me}]^-$) ↔ (LS-$[Fe^{II}H_3L^{Me}]^{2+}$ + LS-$[Fe^{II}L^{Me}]^-$) SCO. In agreement with the rationale that the stronger ligand field supplied to Fe^{II} by the deprotonated L^{Me} ligand compared to the neutral H_3L^{Me} is likely to favor the LS Fe^{II} state, Fe(2) which belongs to the component with the neutral ligand, $[Fe^{II}H_3L^{Me}]^{2+}$, has a transition temperature lower than Fe(1) which belongs to the component with the deprotonated

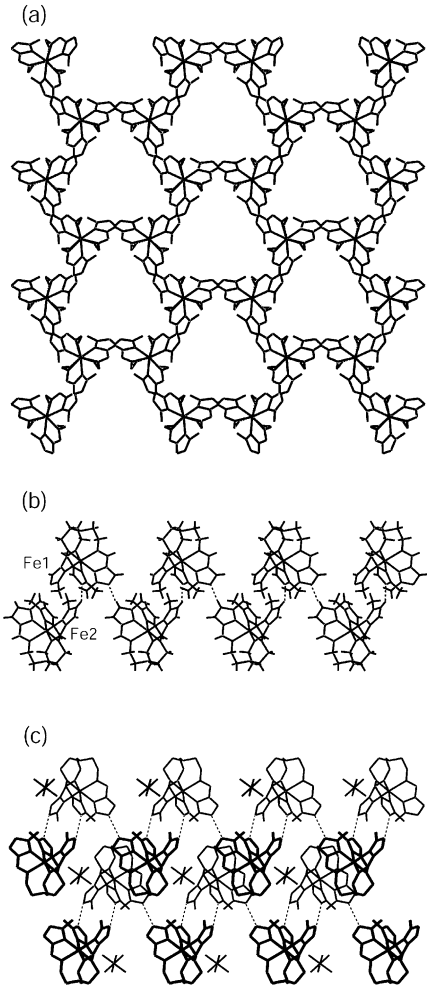

Figure 2. X-ray structure of $[Fe^{II}H_3L^{Me}][Fe^{II}L^{Me}]PF_6$ (**3**) at 295 K. (a) Projection on the *ab*-plane showing a homochiral 2D sheet in which $[Fe^{II}H_3L^{Me}]^{2+}$ and $[Fe^{II}L^{Me}]^{-}$ components with like chirality are linked together by intermolecular imidazole−imidazolate hydrogen bonds. (b) Side view of a puckered sheet looking along the *a*-axis. In this 2D supramolecular structure, the capped tripodlike $[Fe^{II}H_3L^{Me}]^{2+}$ and $[Fe^{II}L^{Me}]^{-}$ components are alternately arrayed in an up-and-down mode. (c) Stacking arrangement of the homochiral puckered sheets along the *c*-axis. The anions are located between the layers.

ligand, $[Fe^{II}L^{Me}]^{-}$. This result is also consistent with the deprotonation process which proceeds from the HS $[Fe^{II}H_3L^{Me}]^{2+}$ to the LS $[Fe^{III}L^{Me}]$ species in solution.[9b] As demonstrated in the previous report,[9b] the spin and oxidation states may be tuned by the degree of deprotonation at the imidazole moiety: deprotonation triggers the HS → LS and $Fe^{II} \rightarrow Fe^{III}$ changes.

Magnetic Properties. The magnetic susceptibilities of polycrystalline samples of compounds **1**−**5** were measured in the 5−300 K temperature range, at 1 K min^{-1} sweeping rate, in a 1 T applied magnetic field. The sample was quickly cooled from room temperature down to 5 K, and the magnetic susceptibility was first measured in the warming mode from 5 to 300 K. Subsequently, the magnetic susceptibility was measured in the cooling mode from 300 to 5 K. The magnetic behaviors in the warming and cooling modes are very similar for all compounds, indicating that there is no frozen-in effect. The magnetic behaviors of **1**−**5** exhibit a two-step SCO,[7g,14] and they may be classified into two groups, (**1** and **2**) and (**3**, **4**, and **5**), on the basis of their $\chi_M T$ vs T curves.

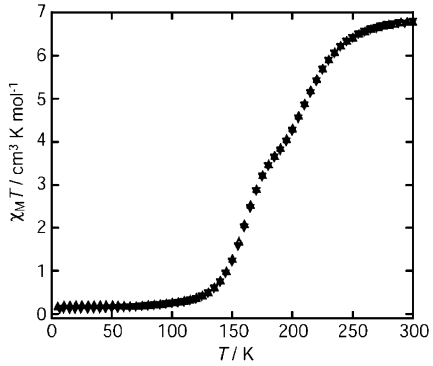

Figure 3. Magnetic behavior of $[Fe^{II}H_3L^{Me}][Fe^{II}L^{Me}]ClO_4$ (**1**) in the form of $\chi_M T$ vs T plots in the warming and cooling modes. The sample was quickly cooled from 300 to 5 K, and χ_M was first measured upon warming from 5 to 300 K at 1 K min^{-1} sweep rate (▲). Subsequently, χ_M was measured upon cooling from 300 to 5 K at 1 K min^{-1} sweep rate (▼).

Magnetic Properties of $[Fe^{II}H_3L^{Me}][Fe^{II}L^{Me}]ClO_4$ (1) and $[Fe^{II}H_3L^{Me}][Fe^{II}L^{Me}]BF_4$ (2). The magnetic behaviors of **1** and **2** being very similar, only the magnetic behavior of **1** is described in detail here. Figure 3 shows the $\chi_M T$ vs T plots for **1**, in which χ_M is the molar magnetic susceptibility per 2Fe and T is the absolute temperature. The $\chi_M T$ curve shows a two-step SCO. Upon lowering the temperature, $\chi_M T$ decreases from ca. 6.8 cm^3 K mol^{-1} at 300 K to 0.2 cm^3 K mol^{-1} at 5 K with an intermediate plateau at ca. 160−180 K. The $\chi_M T$ value of ca. 6.8 cm^3 K mol^{-1} in the 250−300 K range is close to the value expected for two HS Fe^{II} ($S = 2$). The $\chi_M T$ value of ca. 0.2 cm^3 K mol^{-1} below 120 K agrees with that for two LS Fe^{II} ($S = 0$). The $\chi_M T$ value of 3.6 cm^3 K mol^{-1} in the intermediate temperature range is approximately $^1/_2$ of 6.8 cm^3 K mol^{-1}. The magnetic susceptibility data agree with a two-step (HS-$[Fe^{II}H_3L^{Me}]^{2+}$ + HS-$[Fe^{II}L^{Me}]^{-}$) ↔ (HS-$[Fe^{II}H_3L^{Me}]^{2+}$ + LS-$[Fe^{II}L^{Me}]^{-}$) ↔ (LS-$[Fe^{II}H_3L^{Me}]^{2+}$ + LS-$[Fe^{II}L^{Me}]^{-}$) SCO.

Magnetic Properties of $[Fe^{II}H_3L^{Me}][Fe^{II}L^{Me}]PF_6$ (3). The magnetic behaviors of **3**−**5** are essentially similar to each other. Figure 4 shows the $\chi_M T$ vs T plots for **3**. The $\chi_M T$ curve shows two well-separated steps in this SCO. Upon lowering the temperature, $\chi_M T$ decreases from ca. 6.7 cm^3 K mol^{-1} at 300 K to nearly zero at 5 K with an intermediate plateau region between 180 and 220 K. The $\chi_M T$ value of ca. 6.7 cm^3 K mol^{-1} at 300 K is close to the value expected for two HS Fe^{II} ($S = 2$). The $\chi_M T$ value of ca. 0.05 cm^3 K mol^{-1} below 120 K is close to the value expected for two LS Fe^{II} ($S = 0$). The $\chi_M T$ value of ca. 3.5 cm^3 K mol^{-1} in the intermediate temperature range is approximately $^1/_2$ of 6.7 cm^3 K mol^{-1}, indicating that one over two Fe^{II} sites is converted from the HS to the LS Fe^{II} state. The $\chi_M T$ values at the inflection points (obtained from the first derivative of the $\chi_M T$ vs T plots) are 1.8 cm^3 K mol^{-1}at 165 K and 4.7 cm^3 K mol^{-1} at 235 K, i.e., approximately $^1/_4$ and $^3/_4$ of the 300 K $\chi_M T$ value. The magnetic susceptibility data thus

(14) (a) Letard, J.-F.; Real, J. A.; Moliner, N.; Gaspar, A. B.; Capes, L.; Cador, O.; Kahn, O. *J. Am. Chem. Soc.* **1999**, *121*, 10630−10631. (b) Simaan, A. J.; Boillot, M.-L.; Riviere, E.; Boussac, A.; Girerd, J.-J. *Angew. Chem., Int. Ed.* **2000**, *39*, 196−198.

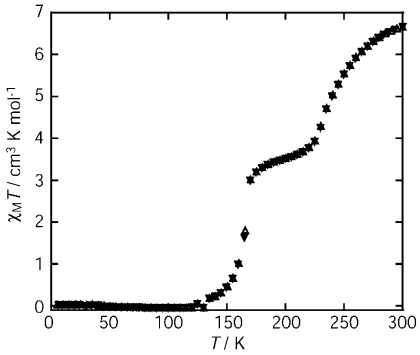

Figure 4. Magnetic behavior of $[Fe^{II}H_3L^{Me}][Fe^{II}L^{Me}]PF_6$ (**3**) in the form of $\chi_M T$ vs T plots in the warming and cooling modes. The sample was quickly cooled from 300 to 5 K, and the χ_M was first measured upon warming from 5 to 300 K at 1 K min^{-1} sweep rate (▲). Subsequently, χ_M was measured upon cooling from 300 to 5 K at 1 K min^{-1} sweep rate (▼).

demonstrate a two-step SCO. Considering the X-ray analyses at 295, 200, and 100 K, we conclude to the occurrence of the two-step (HS-$[Fe^{II}H_3L^{Me}]^{2+}$ + HS-$[Fe^{II}L^{Me}]^-$) ↔ (HS-$[Fe^{II}H_3L^{Me}]^{2+}$ + LS-$[Fe^{II}L^{Me}]^-$) ↔ (LS-$[Fe^{II}H_3L^{Me}]^{2+}$ + LS-$[Fe^{II}L^{Me}]^-$) SCO. The $[Fe^{II}L^{Me}]^-$ component with the deprotonated ligand experiences the SCO process at higher temperature, and the $[Fe^{II}H_3L^{Me}]^{2+}$ component with the neutral ligand experiences the SCO process at lower temperature. It is noteworthy that this second step, involving $[Fe^{II}H_3L^{Me}]^{2+}$, is steeper than the high temperature one.

Mössbauer Spectra of $[Fe^{II}H_3L^{Me}][Fe^{II}L^{Me}]ClO_4$ (1). The temperature dependence of the Mössbauer spectra of **1** was investigated in the 78−300 K range. The sample was initially cooled to 78 K within 3 min, and the Mössbauer spectrum was measured successively in the warming and cooling modes. The Mössbauer spectra in the warming and cooling modes are nearly the same, showing that there is no frozen-in effect. Representative spectra are shown in Figure 5. At 298 K, the spectrum consists of a doublet assignable to HS Fe^{II} (isomer shift $\delta = 0.97$ mm s^{-1} and quadruple splitting $\Delta E_Q = 1.58$ mm s^{-1}). Unexpectedly, the Mössbauer doublets of the differently charged $[Fe^{II}H_3L^{Me}]^{2+}$ and $[Fe^{II}L^{Me}]^-$ components are superimposed. A significant charge delocalization among the bulky $[FeH_3L^{Me}]^{2+}$ and $[FeL^{Me}]^-$ components may result from the extended imidazole−imidazolate hydrogen bond network between the $[Fe^{II}H_3L^{Me}]^{2+}$ cations and $[Fe^{II}L^{Me}]^-$ anions (see the crystal structure of the analogous PF_6^- salt). This charge spreading (spatially similar for $[Fe^{II}H_3L^{Me}]^{2+}$ and $[Fe^{II}L^{Me}]^-$) is likely to be responsible for the closeness of the Mössbauer parameters of these ferrous sites. At 78 K, the spectrum consists of a main quadruple-split LS Fe^{II} doublet ($\delta = 0.47$ mm s^{-1}, $\Delta E_Q = 0.20$ mm s^{-1}) and a low-intensity doublet due to residual HS Fe^{II} ($\delta = 1.31$ mm s^{-1}, $\Delta E_Q = 1.89$ mm s^{-1}). Upon lowering the sample temperature from 298 K, the relative intensity of the doublet due to HS Fe^{II} species decreases, while that due to LS Fe^{II} appears and increases. A deconvolution analysis of the spectra was performed in order to determine the HS vs total Fe^{II} molar fraction, n_{HS}. The Mössbauer parameters are gathered in Table 3, and the plots of the n_{HS} variation with temperature derived from the Mössbauer spectra are shown in Figure 6, together with the

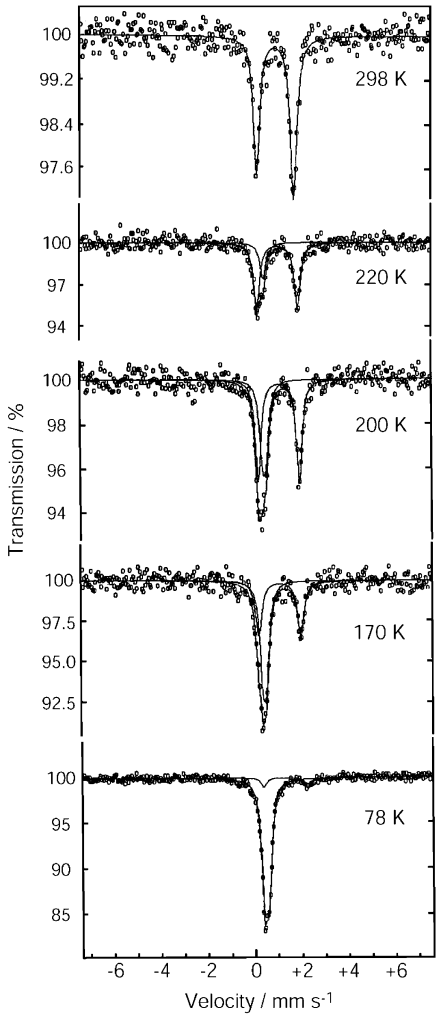

Figure 5. Selected ^{57}Fe Mössbauer spectra of $[Fe^{II}H_3L^{Me}][Fe^{II}L^{Me}]ClO_4$ (**1**) recorded at 78, 170, 200, 220, and 298 K upon warming the sample after rapid cooling to 78 K.

n_{HS} variation derived from the magnetic susceptibility measurements. The plots are nearly the same for the warming and cooling modes, showing a two-step SCO with three plateau regions. The LS Fe^{II} molar ratio does not reach zero, but 0.1, at low temperature. The Mössbauer and magnetic susceptibility results are consistent and confirm the two-step (HS-$[Fe^{II}H_3L^{Me}]^{2+}$ + HS-$[Fe^{II}L^{Me}]^-$) ↔ (HS-$[Fe^{II}H_3L^{Me}]^{2+}$ + LS-$[Fe^{II}L^{Me}]^-$) ↔ (LS-$[Fe^{II}H_3L^{Me}]^{2+}$ + LS-$[Fe^{II}L^{Me}]^-$) SCO.

Mössbauer Spectra of $[Fe^{II}H_3L^{Me}][Fe^{II}L^{Me}]PF_6$ (3). Representative Mössbauer spectra of **3** are shown in Figure 7: they are nearly the same in the warming and cooling modes. At 298 K, the spectrum consists of a HS Fe^{II} doublet ($\delta = 0.97$ mm s^{-1}, $\Delta E_Q = 1.56$ mm s^{-1}). Similarly to the case of **1**, the Mössbauer doublets of the differently charged $[Fe^{II}H_3L^{Me}]^{2+}$ and $[Fe^{II}L^{Me}]^-$ components are superimposed: the same rationale, a significant charge delocalization among the bulky $[FeH_3L^{Me}]^{2+}$ and $[FeL^{Me}]^-$ components may explain the closeness of the Mössbauer parameters of these ferrous sites. At 78 K, the spectrum consists of a LS Fe^{II} doublet ($\delta = 0.48$ mm s^{-1}, $\Delta E_Q = 0.20$ mm s^{-1}). The spectrum at 200 K consists of two quadruple-split doublets

Table 3. Mössbauer Parameters for $[Fe^{II}H_3L^{Me}][Fe^{II}L^{Me}]ClO_4$ (**1**)

T/K	δ^a/mm·s^{-1}	ΔE_Q/mm·s^{-1}	Γ^b/mm·s^{-1}	relative area/%
Warming Mode after Rapid Cooling to 78 K				
298	0.97	1.58	0.33	100
260	1.01	1.69	0.31	95
	0.40	0.10	0.24	5
240	1.03	1.72	0.30	88
	0.43	0.10	0.24	12
220	1.05	1.72	0.32	78
	0.45	0.14	0.28	22
200	1.07	1.76	0.29	62
	0.44	0.16	0.28	38
180	1.09	1.76	0.34	57
	0.45	0.17	0.29	43
170	1.09	1.78	0.34	45
	0.44	0.16	0.29	55
150	1.10	1.80	0.40	27
	0.45	0.18	0.26	73
120	1.23	1.81	0.26	11
	0.46	0.20	0.29	89
78	1.31	1.89	0.26	9
	0.47	0.20	0.29	91
Cooling Mode (Slow) from Room Temperature				
220	1.05	1.72	0.31	77
	0.46	0.12	0.28	23
200	1.07	1.74	0.31	64
	0.45	0.18	0.29	36
180	1.08	1.77	0.32	59
	0.46	0.17	0.29	41
150	1.09	1.80	0.38	25
	0.44	0.18	0.26	75
120	1.20	1.80	0.25	9
	0.48	0.23	0.26	91
78	1.29	1.87	0.25	10
	0.47	0.21	0.29	90

[a] Isomer shift refers to iron foil at 293 K. [b] Full width at half-height.

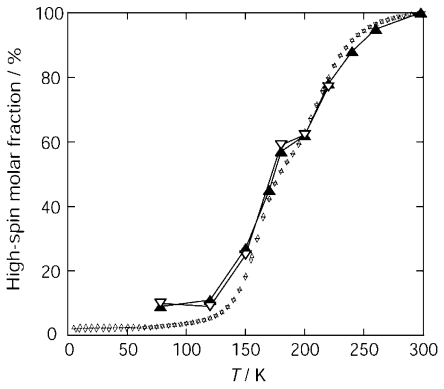

Figure 6. Molar fraction of HS vs total Fe^{II}, n_{HS}, for $[Fe^{II}H_3L^{Me}][Fe^{II}L^{Me}]ClO_4$ (**1**) in the warming (▲) and cooling modes (▼) obtained by deconvolution analysis of the Mössbauer spectra, together with n_{HS} obtained by magnetic susceptibility measurements. n_{HS} was calculated by using the equation $(\chi_M T)_{obs} = n_{HS}(\chi_M T)_{HS} + (1 - n_{HS})(\chi_M T)_{LS}$, with $(\chi_M T)_{HS} = 6.8$ cm^3 K mol^{-1} and $(\chi_M T)_{LS} = 0.0$ cm^3 K mol^{-1} as limiting values.

assigned to LS ($\delta = 0.42$ mm s^{-1}, $\Delta E_Q = 0.19$ mm s^{-1}) and HS Fe^{II} ($\delta = 1.04$ mm s^{-1}, $\Delta E_Q = 1.75$ mm s^{-1}), with equal areas. The deconvolution analysis of the spectra yielded the n_{HS} molar fraction at each temperature. These Mössbauer parameters are gathered in Table 4, and the plots of the n_{HS} variation with temperature derived from the Mössbauer spectra, and magnetic susceptibility measurements, are shown in Figure 8. The plots of the Mössbauer data are nearly the same for the warming and cooling modes, and the plots of the Mössbauer and magnetic susceptibility data are also nearly the same, showing a two-step SCO with three plateau

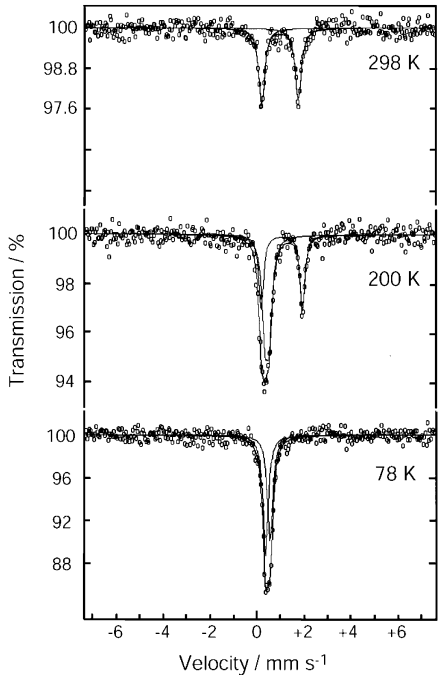

Figure 7. (a) Selected ^{57}Fe Mössbauer spectra of $[Fe^{II}H_3L^{Me}][Fe^{II}L^{Me}]PF_6$ (**3**) recorded at 78, 200, and 298 K upon warming the sample after rapid cooling to 78 K.

Table 4. Mössbauer Parameters for $[Fe^{II}H_3L^{Me}][Fe^{II}L^{Me}]PF_6$ (**3**)

T/K	δ^a/mm·s^{-1}	ΔE_Q/mm·s^{-1}	Γ^b/mm·s^{-1}	relative area/%
Warming Mode after Rapid Cooling to 4.2 K				
298	0.97	1.56	0.32	100
260	1.01	1.69	0.31	95
	0.40	0.10	0.24	5
250	1.01	1.68	0.34	72
	0.41	0.16	0.32	28
230	1.04	1.73	0.27	52
	0.42	0.18	0.29	48
220	1.03	1.72	0.26	48
	0.42	0.18	0.28	52
200	1.04	1.75	0.26	47
	0.42	0.19	0.28	53
180	1.06	1.76	0.28	47
	0.44	0.17	0.28	53
170	1.06	1.78	0.29	40
	0.45	0.18	0.29	60
160	1.12	1.80	0.24	14
	0.46	0.19	0.28	86
150	1.16	1.78	0.22	5
	0.46	0.19	0.27	95
78	0.48	0.20	0.28	100

[a] Isomer shift refers to iron foil at 293 K. [b] Full width at half-height.

regions. The Mössbauer and magnetic susceptibility results are consistent and confirm the two-step (HS-$[Fe^{II}H_3L^{Me}]^{2+}$ + HS-$[Fe^{II}L^{Me}]^-$) ↔ (HS-$[Fe^{II}H_3L^{Me}]^{2+}$ + LS-$[Fe^{II}L^{Me}]^-$) ↔ (LS-$[Fe^{II}H_3L^{Me}]^{2+}$ + LS-$[Fe^{II}L^{Me}]^-$) SCO.

LIESST and Reverse-LIESST Effects of $[Fe^{II}H_3L^{Me}][Fe^{II}L^{Me}]BF_4$ (2). Figure 9a shows the time dependence of the $\chi_M T$ value during the light irradiation at 5 K. The sample was irradiated with various wavelengths (450, 500, 550, 600, 640 nm) selected through interference filter with 80 nm fwhm and with a diode laser light (806 nm). The light irradiation afforded an increase in the $\chi_M T$ value leading to the saturation, which is attributed to the LS to HS SCO of Fe^{II}, the so-called LIESST (light induced excited spin state

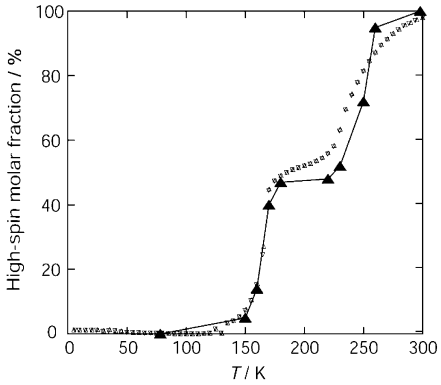

Figure 8. Molar fraction of HS vs total Fe^{II}, n_{HS}, for $[Fe^{II}H_3L^{Me}][Fe^{II}L^{Me}]$-$PF_6$ (**3**) in the warming (▲) mode obtained by deconvolution analysis of the Mössbauer spectra, together with n_{HS} obtained by magnetic susceptibility measurements. n_{HS} was calculated by using the equation $(\chi_M T)_{obs} = n_{HS}(\chi_M T)_{HS} + (1 - n_{HS})(\chi_M T)_{LS}$, with $(\chi_M T)_{HS} = 6.8$ cm^3 K mol^{-1} and $(\chi_M T)_{LS} = 0.0$ cm^3 K mol^{-1} as limiting values.

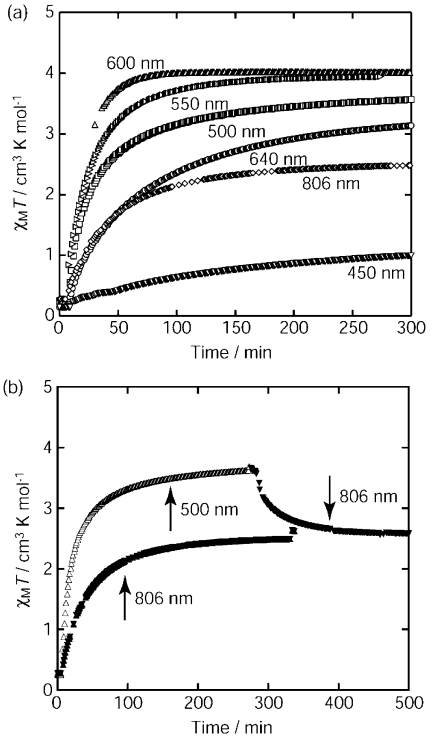

Figure 9. LIESST and reverse-LIESST effects for $[Fe^{II}H_3L^{Me}][Fe^{II}L^{Me}]$-$BF_4$ (**2**). (a) Time dependence of $\chi_M T$ during light irradiation with various wavelengths through an interference filter with 80 nm fwhm ($\lambda_{max} = 450$, 500, 550, 600, 640 nm), and during irradiation with red laser light (806 nm) at 5 K. (b) Time dependence of $\chi_M T$ during light irradiation at 500 nm showing the LIESST effect and then at 806 nm showing the reverse-LIESST effect. Time dependence of $\chi_M T$ during light irradiation with red laser light (806 nm) of the LS sample (LS Fe^{II} + LS Fe^{II}), showing the LIESST effect.

trapping). The shape of the photoexcitation curves is not exponential. The saturation value depends on the wavelength: the light with maximum wavelength (600 nm) is the most effective, yielding a $\chi_M T$ saturation value of ca. 4.0 cm^3 K mol^{-1}, larger than the value expected for 1:1 LS/HS Fe^{II}, and smaller than the value expected for two HS Fe^{II}. Figure 9b shows that the red laser light irradiation ($\lambda = 806$ nm) is effective for both the LIESST and reverse-LIESST effects. After the sample was irradiated with the 500 nm light leading to the HS state (with saturation), the sample was

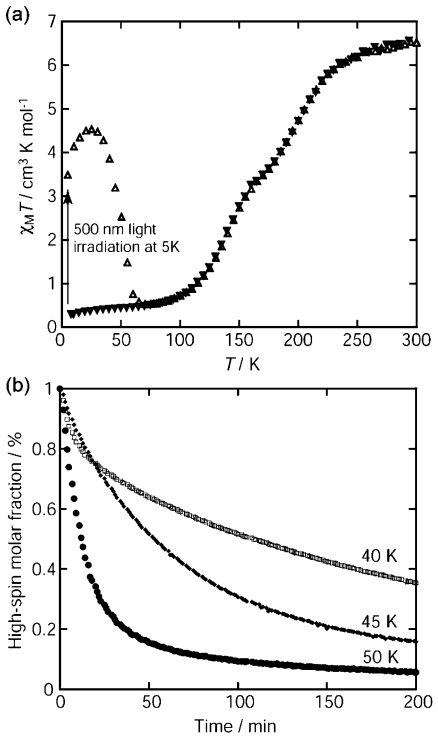

Figure 10. Thermal relaxation process of $[Fe^{II}H_3L^{Me}][Fe^{II}L^{Me}]BF_4$ (**2**). (a) After the light irradiation ($\lambda_{max} = 500$ nm) was switched off, the thermal relaxation process was recorded in the warming mode (▲), χ_M was then measured in the cooling mode from 300 to 5 K (▼). (b) Time dependence at various temperatures of the normalized HS molar fraction, n_{HS}, generated by thermal quenching for $[Fe^{II}H_3L^{Me}][Fe^{II}L^{Me}]BF_4$ (**2**).

subsequently irradiated with the red laser light, inducing a $\chi_M T$ decrease, due to partial HS to LS Fe^{II} SCO, the so-called reverse-LIESST. When the resting (LS-$[Fe^{II}H_3L^{Me}]^{2+}$ + LS-$[Fe^{II}L^{Me}]^{-}$) sample was irradiated with red laser light, the $\chi_M T$ value increased due to partial LS to HS Fe^{II} spin-transition, the so-called LIESST effect. With laser light irradiation, the $\chi_M T$ values reached from a previously saturated state (downward curve) and from the resting state (upward curve) are exactly the same. This phenomenon can be rationalized by considering the intersystem crossing phenomenon proposed by Hauser.[15] Varret and co-workers have studied the time dependence of the population of the excited state following light irradiation either from a previously saturated state (downward curve) or from the resting state (upward curve) and quantitatively explained the light-driven equilibrium.[16]

Figure 10a,b shows the thermal relaxation process after switching off the green light (500 nm). In Figure 10a, the thermal relaxation process was studied by monitoring the $\chi_M T$ value upon warming the sample. Upon raising the temperature from 5 K, the $\chi_M T$ value increases from ca. 4.0 cm^3 K mol^{-1} at 5 K to the maximum value of 5.0 cm^3 K mol^{-1} at 25 K and then decreases abruptly around 50 K. This $\chi_M T$ increase is most probably due to the zero-field splitting of the $S = 2$ ground state of the trapped HS Fe^{II}

(15) Hauser, A. *J. Chem. Phys.* **1991**, *94*, 2741−2748.
(16) Enachescu, C.; Constant-Machado, H.; Codjovi, E.; Linares, J.; Boukheddaden, K.; Varret, F. *J. Phys. Chem. Solids* **2001**, *62*, 1409−1422.

molecules. In the 45−62 K temperature range, $\chi_M T$ diminishes as a consequence of HS → LS relaxation. The results suggest that both Fe^{II} sites of $[Fe^{II}H_3L^{Me}][Fe^{II}L^{Me}]BF_4$ exhibit the LIESST effect. The $[Fe^{II}H_3L^{Me}](BF_4)_2$ HS precursor complex exhibits a weak broad band at 870 nm (ϵ = 10 M^{-1} cm^{-1}) assigned to the $^5T_2 \rightarrow {}^5E$ transition, together with an intense band at λ_{max} = 430 nm (ϵ = 1100 M^{-1} cm^{-1}) assigned to MLCT. Therefore, the red laser light (λ_{max} = 806 nm) can induce the $^5T_2 \rightarrow {}^5E$ transition allowing occurrence of the reverse-LIESST. The $^1A_1 \rightarrow {}^1T_1$ and $^1A_1 \rightarrow {}^1T_2$ LS Fe^{II} transitions are expected at ca. 380 and 550 nm with a molar extinction coefficient of ca. 30 M^{-1} cm^{-1}, on the basis of the spectra observed for LS Fe^{II} complexes with analogous N_6 donor sets.[17]

Figure 10b shows the time dependence at several temperatures of the normalized HS molar fraction, n_{HS}, generated by thermal quenching for $[Fe^{II}H_3L^{Me}][Fe^{II}L^{Me}]BF_4$ (**2**). There is a problem in estimating the normalized HS molar fraction, because the $\chi_M T$ value changes with the increase of the temperature and with time. A single-exponential law did not reproduce the time dependence.

LIESST Effect of $[Fe^{II}H_3L^{Me}][Fe^{II}L^{Me}]AsF_6$ (4). The samples of compounds **3**−**5** were irradiated with green (λ_{max} = 500 nm) and orange light (λ_{max} = 600 nm) at 5 K under the same experimental conditions as for **2**. Compounds **3**−**5** showed no remarkable increase in the $\chi_M T$ value upon light irradiation. Compound **4** showed a small detectable LIESST effect. When the sample was irradiated with green (λ_{max} = 500 nm) or orange light (λ_{max} = 600 nm) at 5 K, a slight increase in the $\chi_M T$ value, attributed to the LS to HS spin-transition, was observed. The orange light irradiation was slightly more efficient than the green one. The orange light irradiation at 5 K yields a $\chi_M T$ saturation value of ca. 1 cm^3 K mol^{-1}, far from the expected value of ca. 3.5 cm^3 K mol^{-1} for (LS-$[Fe^{II}H_3L^{Me}]^{2+}$ + HS-$[Fe^{II}L^{Me}]^-$) or 7.0 cm^3 K mol^{-1} for (HS-$[Fe^{II}H_3L^{Me}]^{2+}$ + HS-$[Fe^{II}L^{Me}]^-$). Furthermore, when the orange light was switched off at 5 K, the $\chi_M T$ value decreased with time. The green light irradiation at 5 K and the thermal relaxation process are shown in Figure 11.

Concluding Remarks. A series of two-dimensional (2D) SCO complexes, $[Fe^{II}H_3L^{Me}][Fe^{II}L^{Me}]X$ (**1**−**5**), $X^- = ClO_4^-$, BF_4^-, PF_6^-, AsF_6^-, SbF_6^-, has been obtained by a one-pot assembly reaction of the corresponding programmed single molecule $[Fe^{II}H_3L^{Me}]X_2$ or $[Fe^{II}H_3L^{Me}]Cl\cdot X$. The crystal structure of $[Fe^{II}H_3L^{Me}][Fe^{II}L^{Me}]PF_6$ (**3**) has been determined at 295, 200, and 100 K, in order to gain insight into the SCO behavior of the compounds in this series. The structure consists of homochiral extended 2D puckered sheets in which the complementary capped tripodlike components $[Fe^{II}H_3L^{Me}]^{2+}$ and $[Fe^{II}L^{Me}]^-$, connected by imidazole−imidazolate hydrogen bonds, are alternately arrayed in an up-and-down mode. Furthermore, the 2D sheets are stacked parallel to each other so as to adapt the puckered shape, and the anion is located between the 2D puckered sheets. An interlayer elastic interaction due to the anion size is one of the important factors governing the SCO behavior for this series of 2D compounds. The temperature dependent magnetic susceptibilities and Mössbauer spectra, together with the X-ray analyses of **3** at three temperatures, revealed that compounds **1**−**5** exhibit a two-step (HS-$[Fe^{II}H_3L^{Me}]^{2+}$ + HS-$[Fe^{II}L^{Me}]^-$) ↔ (HS-$[Fe^{II}H_3L^{Me}]^{2+}$ + LS-$[Fe^{II}L^{Me}]^-$) ↔ (LS-$[Fe^{II}H_3L^{Me}]^{2+}$ + LS-$[Fe^{II}L^{Me}]^-$) SCO, where $[Fe^{II}L^{Me}]^-$ experiences SCO in the higher temperature range and the protonated component $[Fe^{II}H_3L^{Me}]^{2+}$ experiences SCO in the lower temperature range. The SCO curve depends on the size of the counteranion. The onset of the second SCO of the ClO_4^- (**1**) and BF_4^- (**2**) salts adjoins the first SCO, while a mixed (HS-$[Fe^{II}H_3L^{Me}]^{2+}$ + LS-$[Fe^{II}L^{Me}]^-$) spin state spans a temperature range as wide as 70 K for the salts **3**−**5** with larger counteranions, PF_6^-, AsF_6^-, and SbF_6^-, respectively. The LIESST effect was effectively observed for **1** and **2**, whereas the LIESST effect of **3**−**5** is difficult to detect. The larger size of the counteranion separates the first and second SCO well. These distinct differences of the LIESST effect and $\chi_M T$ vs T curve may be ascribed to the size of the counteranion.

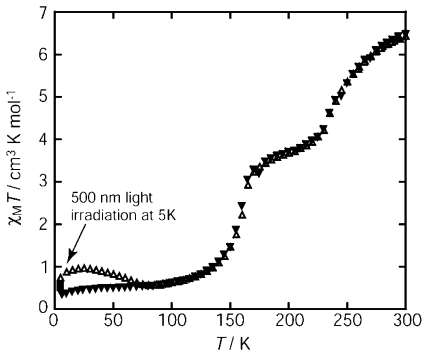

Figure 11. LIESST experiment for $[Fe^{II}H_3L^{Me}][Fe^{II}L^{Me}]AsF_6$ (**4**), thermal relaxation process. After light irradiation (λ_{max} = 500 nm) was switched off, the thermal relaxation process was recorded in the warming mode from 5 to 300 K (▲), and χ_M was then measured in the cooling mode from 300 to 5 K (▼).

Experimental Section

Materials. All chemicals and solvents, obtained from Tokyo Kasei Co., Ltd., and Wako Pure Chemical Industries, Ltd., were reagent grade. They were used without further purification. Reagents used for the physical measurements were of spectroscopic grade.

Tris-[2-(((2-methylimidazol-4-yl)methylidene)amino)ethyl]-amine, H_3L^{Me}. Tris(2-aminoethyl)amine (0.731 g, 5 mmol) was added to a solution of 2-methyl-4-formylimidazole (1.65 g, 15 mmol) in 20 mL of methanol, and the mixture was stirred at 50 °C for 10 min. The methanolic solution of the tripod-type ligand thus prepared was used without isolation for the synthesis of the metal complexes.

$[Fe^{II}H_3L^{Me}](ClO_4)_2$ (1a). To the tripodlike ligand solution (5 mmol) was added a solution of $Fe^{II}Cl_2\cdot 4H_2O$ (0.99 g, 5 mmol) in 20 mL of methanol and then a solution of $NaClO_4$ (1.22 g, 10 mmol) in 20 mL of methanol. The mixture was refluxed and stirred overnight and then filtered. The filtrate was allowed to stand for several days, during which time orange crystals precipitated. They were collected by suction filtration, washed with a small volume

(17) (a) Hinek, R.; Spiering, H.; Schollmeyer, D.; Gütlich, P.; Hauser, A. *Chem. Eur. J.* **1996**, *2*, 1427−1434. (b) Jeftic, J.; Hinek, R.; Capelli, S. C.; Hauser, A. *Inorg. Chem.* **1997**, *36*, 3080−3087. (c) Al-Obaidi, A. H. R.; Jensen, K. B.; McGarvey, J. J.; Toftlund, H.; Jensen, B.; Bell, S. E. J.; Carroll, J. G. *Inorg. Chem.* **1996**, *35*, 5055−5060.

of methanol, and dried in vacuo. Recrystallization was performed from the methanol solution containing a small amount of HCl. Yield: 0.65 g (19%). Anal. Calcd for $[Fe^{II}H_3L^{Me}](ClO_4)_2$: C 37.24, H 4.46, N 20.68. Found: C 37.52, H 4.66, N 20.82. IR(KBr): $\nu_{C=N}$ 1639 cm^{-1}, $\nu_{Cl-O}(ClO_4^-)$ 1080, 1049 cm^{-1}.

$[Fe^{II}H_3L^{Me}](BF_4)_2 \cdot 0.5MeOH$ (2a). This complex was prepared similarly to **1a**, using $NaBF_4$ instead of $NaClO_4$. Orange crystals were obtained with a 22% yield. Anal. Calcd for $[Fe^{II}H_3L^{Me}](BF_4)_2 \cdot 0.5MeOH$: C 38.66, H 4.83, N 20.96. Found: C 38.64, H 4.91, N 21.24. IR(KBr): $\nu_{C=N}$ 1640 cm^{-1}, $\nu_{B-F}(BF_4^-)$ 1082 cm^{-1}.

$[Fe^{II}H_3L^{Me}]Cl \cdot PF_6 \cdot MeOH$ (3a). To the ligand solution (5 mmol) was added a solution of $Fe^{II}Cl_2 \cdot 4H_2O$ (0.99 g, 5 mmol) in 20 mL of methanol and then a solution of KPF_6 (1.84 g, 10 mmol) in 20 mL of methanol. The mixture was refluxed and stirred on a hot plate overnight and then filtered. The filtrate was allowed to stand for several days, during which time dark-orange crystals precipitated. They were collected by suction filtration, washed with a small volume of methanol, and dried in vacuo. Recrystallization was performed from the methanol solution containing a small amount of HCl. Yield: 22%. Anal. Calcd for $[Fe^{II}H_3L^{Me}]Cl \cdot PF_6 \cdot MeOH$: C 38.25, H 4.96, N 20.28. Found: C 38.30, H 4.91, N 20.32. IR(KBr): $\nu_{C=N}$ 1638 cm^{-1}, $\nu_{P-F}(PF_6^-)$ 842 cm^{-1}.

$[Fe^{II}H_3L^{Me}]Cl \cdot AsF_6 \cdot 0.5MeOH$ (4a) and $[Fe^{II}H_3L^{Me}]Cl \cdot SbF_6 \cdot MeOH$ (5a). These complexes were prepared similarly to **3a**, using $NaAsF_6$ **(4a)** and $NaSbF_6$ **(5a)** instead of KPF_6. Dark-orange crystals were obtained with 25% **(4a)** and 39% **(5a)** yields. Anal. Calcd for $[Fe^{II}H_3L^{Me}]Cl \cdot AsF_6 \cdot 0.5MeOH$ **(4a)**: C 35.92, H 4.48, N 19.49. Found: C 35.95, H 4.58, N 19.57. IR(KBr): $\nu_{C=N}$ 1638 cm^{-1}, $\nu_{As-F}(AsF_6^-)$ 703 cm^{-1}. Anal. Calcd for $[Fe^{II}H_3L^{Me}]Cl \cdot SbF_6 \cdot MeOH$ **(5a)**: C 33.65, H 4.03, N 18.69. Found: C 33.72, H 4.02, N 18.78. IR(KBr): $\nu_{C=N}$ 1640 cm^{-1}, $\nu_{Sb-F}(SbF_6^-)$ 661 cm^{-1}.

$[Fe^{II}H_3L^{Me}][Fe^{II}L^{Me}]ClO_4$ (1). To a warm methanol solution of $[Fe^{II}H_3L^{Me}](ClO_4)_2$ (**1a**) (0.60 g, 0.89 mmol) was added 1 M aqueous KOH (1.5 equiv). The mixture was warmed on a water bath for several hours, during which time the color of the solution gradually changed from yellow-orange to dark-red, and red-black crystals of $[Fe^{II}H_3L^{Me}][Fe^{II}L^{Me}]ClO_4$ (**1**) precipitated. They were collected by suction filtration, washed with a small volume of methanol, and dried in vacuo. Yield: 0.30 g (64%). Anal. Calcd for $[Fe^{II}H_3L^{Me}][Fe^{II}L^{Me}]ClO_4$: C 47.90, H 5.46, N 26.60. Found: C 47.90, H 5.65, N 26.59. IR(KBr): $\nu_{C=N}$ 1635 cm^{-1}, $\nu_{Cl-O}(ClO_4^-)$ 1100, 1082, 1053 cm^{-1}.

$[Fe^{II}H_3L^{Me}][Fe^{II}L^{Me}]BF_4$ (2), $[Fe^{II}H_3L^{Me}][Fe^{II}L^{Me}]PF_6$ (3), $[Fe^{II}H_3L^{Me}][Fe^{II}L^{Me}]AsF_6$ (4), $[Fe^{II}H_3L^{Me}][Fe^{II}L^{Me}]SbF_6 \cdot H_2O$ (5). These complexes were prepared similarly to **1**, using $[Fe^{II}H_3L^{Me}](BF_4)_2 \cdot 0.5MeOH$ (**2a**) for **2**, $[Fe^{II}H_3L^{Me}]Cl \cdot PF_6 \cdot MeOH$ (**3a**) for **3**, $[Fe^{II}H_3L^{Me}]Cl \cdot AsF_6 \cdot 0.5MeOH$ (**4a**) for **4**, and $[Fe^{II}H_3L^{Me}]Cl \cdot SbF_6 \cdot MeOH$ (**5a**) for **5**, instead of **1a**. Red-black crystals were obtained with 57% **(2)**, 73% **(3)**, 66% **(4)**, and 35% **(5)** yields. Anal. Calcd for $[Fe^{II}H_3L^{Me}][Fe^{II}L^{Me}]BF_4$ **(2)**: C 48.48, H 5.52, N 26.92. Found: C 48.24, H 5.48, N 27.07. IR(KBr): $\nu_{C=N}$ 1635 cm^{-1}, $\nu_{B-F}(BF_4^-)$ 1084 cm^{-1}. Anal. Calcd for $[Fe^{II}H_3L^{Me}][Fe^{II}L^{Me}]PF_6$ **(3)**: C 45.91, H 5.23, N 25.50. Found: C 45.72, H 5.11, N 25.63. IR(KBr): $\nu_{C=N}$ 1635 cm^{-1}, $\nu_{P-F}(PF_6^-)$ 849 cm^{-1}. Anal. Calcd for $[Fe^{II}H_3L^{Me}][Fe^{II}L^{Me}]AsF_6$ **(4)**: C 44.15, H 5.03, N 24.52. Found: C 43.87, H 5.03, N 24.60. IR(KBr): $\nu_{C=N}$ 1637 cm^{-1}, $\nu_{As-F}(AsF_6^-)$ 705 cm^{-1}. Anal. Calcd for $[Fe^{II}H_3L^{Me}][Fe^{II}L^{Me}]SbF_6 \cdot H_2O$ **(5)**: C 41.78, H 4.93, N 23.12. Found: C 41.78, H 4.84, N 23.12. IR(KBr): $\nu_{C=N}$ 1638 cm^{-1}, $\nu_{Sb-F}(SbF_6^-)$ 665 cm^{-1}.

Physical Measurements. Elemental C, H, and N analyses were carried out by Miss Kikue Nishiyama at the Center for Instrumental Analysis of Kumamoto University. Infrared spectra were recorded on a Perkin-Elmer FT-IR PARAGON 1000 spectrometer using KBr disks at room temperature. Electronic spectra were recorded on a Shimadzu UV−vis Spectrophotometer UV-2450 at room temperature. Magnetic susceptibilities were measured using a MPMS5 SQUID susceptometer (Quantum Design) in the 5−300 K temperature range, at 1 K min^{-1} sweeping rate, under an applied magnetic field of 1 T. The calibration was carried out with palladium metal. Corrections for diamagnetism were applied using Pascal's constants.[18] For the LIESST and reverse-LIESST experiments, a xenon arc lamp (Hamamatsu L7810) and diode laser (806 nm, ILX Lightwave LDT-5525, LDX-3525) were used as the light sources. The interference filtered light of a xenon arc lamp was guided via an optical fiber into the SQUID magnetometer. The sample was placed at the edge of the optical fiber, where the power of the light is 2 mW cm^{-2}. The measurements were performed on a very thin layer of powdered sample. The weight was estimated by comparing the thermal SCO curve with that for an heavier and accurately weighted sample. The Mössbauer spectra were recorded using a Wissel 1200 spectrometer and a proportional counter. $^{57}Co(Rh)$ moving in a constant acceleration mode was used as radioactive source. The hyperfine parameters were obtained by least-squares fitting to Lorentzian peaks. The isomer shifts are reported relative to metal iron foil at 293 K. The sample temperature was controlled by a Heli-tran liquid transfer refrigerator (Air Products and Chemicals, Inc.) with an accuracy of ±0.5 K.

Crystallographic Data Collection and Structure Determination for $[Fe^{II}H_3L^{Me}][Fe^{II}L^{Me}]PF_6$ (3) at 295, 200, and 100 K. The selected crystal (red prismatic block, 0.40 × 0.25 × 0.10 mm^3) was mounted on an Oxford-Diffraction Xcalibur diffractometer using graphite monochromated Mo Kα radiation ($\lambda = 0.71073$ Å) and equipped with an Oxford Instruments Cryojet cooler device.[19] Three data collections were performed at 295, 200, and 100 K. Data were collected with 4 runs ($\phi = 0°$, 90°, 180°, 270°) and ω scans up to $\theta = 26°$. There were 9397 reflections collected at 295 K, of which 3192 were independent ($R_{int} = 0.0655$), 8943 reflections at 200 K of which 3057 were independent ($R_{int} = 0.0532$), and 8507 reflections at 100 K of which 2906 were independent ($R_{int} = 0.0550$). No absorption corrections were applied. The structures were solved by direct methods using SHELXS-97[20] and refined on F^2 by a full-matrix least-squares method using SHELXL-97[21] with anisotropic displacement parameters for all the non-hydrogen atoms. Scattering factors were taken from ref 22. The PF_6 atoms appeared to be disordered. Occupancy factors were refined in the ratio 50/50 for the structures at 295 and 100 K, and in the ratio 85/15 for the structure at 200 K. Refinement diverged for the data at 200 K, so in this case the disorder was ignored. The imidazole hydrogen atom H(7) and approximately half of all hydrogen atoms were located on the D-Fourier. For consistency, all H atoms were located geometrically for the CIF file, with isotropic thermal parameters 1.1 times higher than those of the riding atom. However, in order to unambiguously identify the cationic and anionic components in this structure, we have refined the imidazole hydrogen atom and obtained the following results allowing to consider the $[Fe^{II}H_3L^{Me}]^{2+}[Fe^{II}L^{Me}]^-(PF_6)^-$ formulation as the most

(18) Kahn, O. *Molecular Magnetism*; VCH: Weinheim, 1993.
(19) Watkin, D. J.; Prout, C. K.; Carruthers, J. R.; Betteridge, P. W. *CRYSTALS* Issue 10; Chemical Crystallography Laboratory: Oxford, U.K., 1996. *CRYSTALS* Version 170. Oxford-Diffraction: Oxford, 2002.
(20) Sheldrick, G. M. *SHELXS-97. Program for Crystal Structure Solution*; University of Göttingen: Göttingen, Germany, 1990.
(21) Sheldrick, G. M. *SHELXL-97. Program for the refinement of crystal structures from diffraction data*; University of Göttingen: Göttingen, Germany, 1997.
(22) *International Tables for Crystallography*; Kluwer Academic Publishers: Dordrecht, The Netherlands, 1992; Vol. C.

plausible chemical formula, at 100 K, located on the D-Fourier: N(7)−H(7) = 1.02 Å; N(3)···H(7) = 1.66 Å; N(7)−H(7)···N(3) = 175°. Refined: N(7)−H(7) = 0.75(5) Å; N(3)···H(7) = 2.02(5) Å; N(7)−H(7)···N(3) = 150(6)°. At 200 K, located on the D-Fourier: N(7)−H(7) = 0.91 Å; N(3)···H(7) = 1.76 Å; N(7)−H(7)···N(3) = 168°. Refined: N(7)−H(7) = 0.90(4) Å; N(3)···H(7) = 1.83(4) Å; N(7)−H(7)···N(3) = 159(3)°. At 295 K located on the D-Fourier: N(7)−H(7) = 0.98 Å; N(3)···H(7) = 1.70 Å; N(7)−H(7)···N(3) = 168°. Refined: N(7)−H(7) = 1.04(17) Å; N(3)···H(7) = 1.71(18) Å; N(7)−H(7)···N(3) = 158(9)°.

Acknowledgment. This work was partly supported by a Grant-in-Aid for Science Research (14340209) from the Ministry of Education, Science, Sports, and Culture, Japan.

Supporting Information Available: X-ray crystallographic file in CIF format for **3** at 295, 200, and 100 K. This material is available free of charge via the Internet at http://pubs.acs.org.

IC034439E